Available online at www.sciencedirect.com
SCIENCE DIRECT®
Journal of Computational Physics 200 (2004) 670–694
JOURNAL OF COMPUTATIONAL PHYSICS
www.elsevier.com/locate/jcp

An efficient, preconditioned, high-order solver for scattering by two-dimensional inhomogeneous media

Oscar P. Bruno [a,1], E. McKay Hyde [b,*,2]

[a] *Applied and Computational Mathematics, Caltech, Pasadena, CA 91125, USA*
[b] *School of Mathematics, University of Minnesota, 127 Vincent Hall, 206 Church Street SE, Minneapolis, MN 55455, USA*

Received 31 October 2003; received in revised form 29 April 2004; accepted 29 April 2004
Available online 8 June 2004

Abstract

We consider the problem of evaluating the scattering of TE polarized electromagnetic waves by two-dimensional penetrable inhomogeneities: building upon previous work [IEEE Trans. Antennas Propag. 48 (2000) 1862] we present a practical and general fast integral equation algorithm for this problem. The contributions introduced in this text include: (1) a preconditioner that significantly reduces the number of iterations required by the algorithm in the treatment of electrically large scatterers, (2) a new radial integration scheme based on Chebyshev polynomial approximation, which gives rise to increased accuracy, efficiency and stability, and (3) an efficient and stable method for the evaluation of scaled high-order Bessel functions, which extends the capabilities of the method to arbitrarily high frequencies. These enhancements give rise to an algorithm that is much more accurate and efficient than its previous counterpart, and that allows for treatment of much larger problems than permitted by the previous approach. In one test case, for example, the present algorithm results in far-field errors of 8.9×10^{-13} in a $2.12s$ calculation (on a 1.7 GHz PC) whereas the original algorithm gave rise to far-field errors of 1.1×10^{-8} in $88.91s$ on a 400 MHz PC. In another example, the present algorithm evaluates accurately the scattering by a cylinder of acoustical size $\kappa R = 256$, which is of the order of 20 times larger (400 times larger in square wavelengths) than the largest scatterers that could be treated by the previous approach. Yielding, at worst, third-order far field accuracy (or substantially better, for smooth scatterers) in fast computing times ($\mathcal{O}(N \log N)$ operations for an N point mesh) even for discontinuous and complex refractive index distributions (possibly containing severe geometric singularities such as corners and cusps), the proposed approach is the highest-order $\mathcal{O}(N \log N)$ solver in existence for the problem under consideration.

AMS: 35J05; 65D30; 65F10; 65N12; 65R20; 65T50; 78A45; 78M25

* Corresponding author. Tel.: +1-612-624-5895; fax: +1-612-626-2017.
E-mail address: hyde@math.umn.edu (E.M. Hyde).

[1] Supported by the AFOSR under Grant Nos. F49620-96-1-0008, F49629-99-1-0010 and F49620-02-10049, by the NSF through the NYI award DMS-9596152 and contract Nos. DMS-9523292, DMS-9816802 and DMS-0104531 and by the Powell Research Foundation.
[2] Supported through a DOE Computational Science Graduate Fellowship, an Achievement Reward for College Scientists (ARCS) Fellowship and an NSF Mathematical Sciences Postdoctoral Research Fellowship.

0021-9991/$ - see front matter
doi:10.1016/j.jcp.2004.04.017

Keywords: Helmholtz equation; Lippmann–Schwinger equation; FFT; TE/TM scattering; Preconditioner; Chebyshev polynomials; Bessel functions

1. Introduction

Scattering problems find application in a wide range of fields including communications, materials science, plasma physics, biology and medicine, radar and remote sensing. The evaluation of useful numerical solutions to such problems remains a challenge, requiring novel mathematical approaches and powerful computational tools. In this paper, building on the contribution of [1,2], we present a practical and general integral equation algorithm for the evaluation of time-harmonic, TE polarized electromagnetic scattering by bounded inhomogeneities in two dimensions. (Note that there is some ambiguity in the naming of the polarization with some authors referring to this setting as TM polarized scattering; see [3–6]. To be precise, we consider the case in which the electric field is parallel to the cylindrical axis of the scatterer.)

Our problem can be stated as follows: given an incident field u^{i}, satisfying $\Delta u^{\mathrm{i}} + \kappa^2 u^{\mathrm{i}} = 0$, we denote by u the total electric field – which equals the sum of u^{i} and the resulting scattered field u^{s}: $u = u^{\mathrm{i}} + u^{\mathrm{s}}$. The refractive index of the scattering obstacle is given by a bounded (possibly discontinuous) function $n(x)$, where $n(x) = 1$ outside some compact set Ω. Calling λ the wavelength of the incident field and $\kappa = 2\pi/\lambda$ the wavenumber, the total field u satisfies [7, p. 2]

$$\Delta u + \kappa^2 n^2(x) u = 0, \quad x \in \mathbb{R}^3. \tag{1}$$

Finally, the scattered field, u^{s}, is required to satisfy the Sommerfeld radiation condition [7, p. 67]

$$\lim_{r\to\infty} \sqrt{r}\left(\frac{\partial u^{\mathrm{s}}}{\partial r} - \mathrm{i}\kappa u^{\mathrm{s}}\right) = 0. \tag{2}$$

An appropriate integral formulation for our two-dimensional TE problem is given by the Lippmann–Schwinger equation [7, p. 214]

$$u(x) = u^{\mathrm{i}}(x) - \kappa^2 \int_{\Omega} g(x-y) m(y) u(y)\, \mathrm{d}y, \tag{3}$$

where $g(x) = (\mathrm{i}/4) H_0^1(\kappa|x|)$ is the fundamental solution for the Helmholtz equation in two dimensions and m is the *compactly supported* function $m = 1 - n^2$. For the present problem, integral equation methods have a number of advantages over, say, finite element methods; in particular, the integral approaches only require discretization of the equation *on the scatterer itself* (the region surrounding the scatterer needs not be discretized), and the solutions they produce satisfy the radiation condition at infinity *automatically* (no absorbing boundary conditions are needed). Direct use of integral equation methods is costly, however, since they lead to dense linear systems of equations: a straightforward computation of the required convolution requires $\mathcal{O}(N^2)$ operations per iteration of an iterative linear solver – where N is the number of mesh points in the discretization. As in other Fourier-based integral methods [8], however, in our integral equation approach the complexity of the convolution evaluation is reduced to $\mathcal{O}(N \log N)$ operations per iteration. In addition, our method achieves *higher-order* accuracy, yielding, at worst, far-field errors of order $\mathcal{O}(h^3)$, even for discontinuous and rather complex refractive index distributions – possibly containing geometric singularities such as corners and cusps, which present severe difficulties for other methods. This compares favorably with previous approaches, which either require $\mathcal{O}(N^2)$ operations per iteration or, if

applicable in $\mathcal{O}(N \log N)$ operations per iteration, yield lower orders of accuracy than our approach – no better than $\mathcal{O}(h^2(1+\log(h)))$ accuracy for discontinuous refractive indexes [8–12] (see [13] for a more detailed comparison of various algorithms for the problem under consideration).

Following [1,2], our method is based on recasting the integral term of (3) in the polar coordinate form

$$(Ku)(a,\phi) = -\kappa^2 \int g(a,\phi;r,\theta) m(r,\theta) u(r,\theta) r \, \mathrm{d}r \, \mathrm{d}\theta. \tag{4}$$

An approximate integral equation is obtained from (4) by replacing the fundamental solution g by a truncation of its Fourier representation with respect to the angular variables (given by the addition theorem for the Hankel function [7, p. 67]). Denoting the solution of the approximate integral equation by v, we have

$$v(a,\phi) = u^{\mathrm{i},M}(a,\phi) + (K^M v)(a,\phi), \tag{5}$$

where

$$u^{\mathrm{i},M}(a,\phi) = \sum_{\ell=-M}^{M} u_\ell^{\mathrm{i}}(a) \mathrm{e}^{\mathrm{i}\ell\phi}, \tag{6}$$

$$(K^M v)(a,\phi) = \sum_{\ell=-M}^{M} (K_\ell v)(a) \mathrm{e}^{\mathrm{i}\ell\phi}. \tag{7}$$

Here, using an annular region $R_0 \leqslant a \leqslant R_1$ containing the support of m, the operator K_ℓ is defined by

$$(K_\ell v)(a) = -\frac{\mathrm{i}\kappa^2}{4} \int_{R_0}^{R_1} \mathscr{J}_\ell(a,r) I_\ell(r) r \, \mathrm{d}r, \tag{8}$$

where calling J_ℓ and H_ℓ^1 the Bessel and Hankel functions of order ℓ,

$$\mathscr{J}_\ell(a,r) = H_\ell^1(\kappa \max(a,r)) \; J_\ell(\kappa \min(a,r)) \tag{9}$$

and

$$I_\ell(r) = \int_0^{2\pi} m(r,\theta) v^M(r,\theta) \mathrm{e}^{-\mathrm{i}\ell\theta} \, \mathrm{d}\theta. \tag{10}$$

From (5) it is clear that $v = v^M$, i.e., the approximate solution v is itself a truncated Fourier series. (Throughout this paper we use a superscript M to denote the truncated Fourier series of order M of a given function.)

Remark 1. Note that the polar coordinate formulation in no way restricts our algorithm to cylindrically symmetric scatterers; indeed, the algorithm can treat a completely general collection of bounded penetrable inhomogeneities. Further, the polar coordinate formulation is particularly well adapted for use in a number of important applications. In particular, fiber optics problems often require the solution of the Helmholtz equation (1) within a disc [14].

In [15,13] we proved that Eq. (5) admits a unique solution v^M for piecewise-smooth inhomogeneities m, and that v^M provides a high-order approximation to the solution u of (3) (see [13] for a more precise definition of the appropriate spaces and a more precise statement of the results). In particular, for a discontinuous and piecewise-smooth inhomogeneity m, the L^∞ error decays as $\mathcal{O}(M^{-3})$ in the far field and as

$\mathcal{O}(M^{-2})$ in the near field; furthermore, the order of convergence increases rapidly with the degree of regularity of m.

Like the algorithm of [1,2], the method presented in this paper is based on consideration of the polar coordinate formulation (5). The contributions introduced in this text include: (1) a new radial integration scheme based on Chebyshev polynomial approximations, which gives rise to increased accuracy, efficiency and stability (Section 3), (2) an efficient and stable method for the evaluation of scaled high-order Bessel functions, which extends the capabilities of the method to arbitrarily high frequencies (Section 4), and (3) a preconditioner that significantly reduces the number of iterations required by the algorithm in the treatment of electrically large scatterers (Section 5). These enhancements give rise to an algorithm that is much more accurate and efficient than its previous counterpart, and that allows for treatment of much larger problems than permitted by the previous approach. In one test case, for example, the present algorithm results in far-field errors of 8.9×10^{-13} in a $2.12s$ calculation (on a 1.7 GHz PC) whereas the original algorithm gave rise to far-field errors of 1.1×10^{-8} in $88.91s$ on a 400 MHz PC. In another example we evaluate scattering by a cylinder of acoustical size $\kappa R = 256$, which of the order of 20 times larger (400 times larger in square wavelengths) than the largest scatterers that could be treated by the previous approach. A variety of numerical examples illustrating the efficiency and accuracy of the method, including applications to refractive index distributions containing complex geometric singularities, are presented in Section 6.

2. High-order angular integration

For high-order, $\mathcal{O}(N \log N)$ evaluation of the quantities $I_\ell(r)$ in Eq. (10) we proceed as in [2]: in terms of the Fourier coefficients of the inhomogeneity m and the approximate solution v^M we have

$$I_\ell(r) = \int_0^{2\pi} \left(\sum_{j=-\infty}^{\infty} m_j(r) \mathrm{e}^{\mathrm{i}j\theta} \right) \left(\sum_{k=-M}^{M} v_k(r) \mathrm{e}^{\mathrm{i}k\theta} \right) \mathrm{e}^{-\mathrm{i}\ell\theta} = 2\pi \sum_{k=-M}^{M} m_{\ell-k}(r) v_k(r), \tag{11}$$

where $\ell = -M, \ldots, M$. Hence, at each radius r, $I_\ell(r)$ is given by a *finite* convolution of the Fourier coefficients $m_\ell(r)$ and $v_\ell(r)$ involving Fourier modes of m of orders $|\ell| \leqslant 2M$. In our method these convolution are evaluated by a well-known FFT algorithm [16, pp. 531–537] at a computational cost of $\mathcal{O}(M \log M)$ for each radius. Therefore, given the finitely many Fourier coefficients $m_\ell(r)$ and $v_\ell(r)$ in (11), we can compute the angular integrals $I_\ell(r)$ *exactly* (except for roundoff errors) in a total of $\mathcal{O}(N_\mathrm{r} M \log M) = \mathcal{O}(N \log N)$ operations, where N_r denotes the number of radial discretization points and $N = N_\mathrm{r}(2M + 1)$ denotes the total number of unknowns.

Note the following interesting implication of (11): the high-order modes of m (m_ℓ for $|\ell| > 2M$) do not enter the calculation of I_ℓ. It follows that the function m can be replaced by the smooth function m^{2M} *with no effect* on the accuracy of I_ℓ. Similarly, it is not difficult to see that, after first replacing m by m^{2M}, evaluation of the convolutions (11) is *exactly* equivalent to trapezoidal rule integration of (10) with $N_\theta > 4M$ integration points. More precisely,

$$I_\ell(r) = I_\ell^{N_\theta}(r) \equiv \sum_{j=0}^{N_\theta - 1} m^{2M}(r, \theta_j) v^M(r, \theta_j) \mathrm{e}^{-2\pi \mathrm{i} j\ell / N_\theta}, \tag{12}$$

where $\theta_j = 2\pi j / N_\theta$ for $j = 0, 1, \ldots, N_\theta - 1$. We thus compute $I_\ell^{N_\theta}(r)$ using FFTs in a total of $\mathcal{O}(N \log N)$ operations.

Although $I_\ell(r)$ may always be computed exactly by replacing m by m^{2M}, in the case of sufficiently smooth inhomogeneities the direct application of the trapezoidal rule is somewhat simpler (since the Fourier coefficients $m_\ell(r)$ are not required) and produces nearly the same accuracy (since the trapezoidal rule yields

high-order accuracy for smooth and periodic integrands [17, p. 288]). Hence, in practice, we use the trapezoidal rule to compute (10), replacing m by m^{2M} only for inhomogeneities with discontinuous low-order derivatives.

3. High-order radial integration: Chebyshev approximation

We now turn to the high-order evaluation of the radial integrals (8), which may be expressed in the form

$$\begin{aligned}(K_\ell v^M)(a) &= -\mathrm{i}\frac{\kappa^2}{4}\left[\int_{R_0}^{a} H_\ell^1(\kappa a)J_\ell(\kappa r)I_\ell(r)r\,\mathrm{d}r + \int_a^{R_1} J_\ell(\kappa a)H_\ell^1(\kappa r)I_\ell(r)r\,\mathrm{d}r\right]\\ &= \frac{\kappa^2}{4}\left[F_\ell^{(1)}(a) + F_\ell^{(2)}(a) - \mathrm{i}\frac{J_\ell(\kappa a)}{Y_\ell(\kappa R_1)}F_\ell^{(1)}(R_1)\right] \end{aligned} \tag{13}$$

for $R_0 \leqslant a \leqslant R_1$ (with a simple modification for the case $Y_\ell(\kappa R_1) = 0$), where

$$F_\ell^{(1)}(a) = \int_{R_0}^{a} Y_\ell(\kappa a)J_\ell(\kappa r)I_\ell(r)r\,\mathrm{d}r, \tag{14}$$

$$F_\ell^{(2)}(a) = \int_a^{R_1} J_\ell(\kappa a)Y_\ell(\kappa r)I_\ell(r)r\,\mathrm{d}r. \tag{15}$$

As indicated in Section 1, our method for evaluation of $F_\ell^{(1)}(a)$ and $F_\ell^{(2)}(a)$ relies on high-order Chebyshev approximation of the functions $I_\ell(r)$. To obtain the desired high-order accurate approximations, it is important to identify and treat any singularities in the function $I_\ell(r)$, which can only arise, in fact, from corresponding singularities in the Fourier coefficients $m_\ell(r)$ of the inhomogeneity.

To provide some details, let us denote by $\mathscr{D}$ any one of the sets with piecewise-smooth boundary within which $m(r,\theta)$ is smooth and such that m is discontinuous on $\partial\mathscr{D}$; in general, singularities in $m_\ell(r)$ occur at points $r = r_0$ for which the circle $r = r_0$ intersects the boundary of such a set $\mathscr{D}$ at (1) a non-smooth point of $\partial\mathscr{D}$, or (2) at a point of tangency between the circle and $\partial\mathscr{D}$, or a combination of these two cases. In case (1), it is easy to check that $m_\ell(r)$ has a corner-type singularity, i.e., $m_\ell(r)$ is smooth on either side of $r = r_0$. In case (2), we have two important subcases. In the first subcase the circle intersects $\partial\mathscr{D}$ at a single point; here one can show that $m_\ell(r)$ has a singularity of type $|r - r_0|^\gamma$ for $0 < \gamma < 1$. In the second subcase the the circle intersects the boundary on an arc; this gives rise to a jump discontinuity in $m_\ell(r)$ on each side of which $m_\ell(r)$ is smooth.

Remark 2. Accurate determination of the values of γ mentioned above and resolution of the corresponding singularity gives rise to significant improvements in the convergence rates; see Table 2. Fortunately, evaluation of such values does not entail any significant difficulty: the short discussion presented in Appendix A shows that γ can be determined simply from the degree of tangency of the circle $r = r_0$ and the boundary of any set $\mathscr{D}$.

To handle these singularities, we first subdivide the domain of integration $[R_0, R_1]$ into several intervals in such a way that the singularities of $m_\ell(r)$ (and hence of $I_\ell(r)$) occur only at endpoints of these intervals. On each interval, we then resolve the remaining singularities, which can only be of type $|r - r_0|^\gamma$, through appropriate changes of variables. For example, on a given interval $[a, b]$, square-root singularities (the most typical in our context) can be resolved by means of the change of variables

$$\cos(\phi) = \sqrt{\frac{r^2 - a^2}{b^2 - a^2}}. \tag{16}$$

Thus, this procedure of breaking the integration domain $[R_0, R_1]$ into multiple intervals and using appropriate changes of variables to resolve $|r - r_0|^\gamma$-type singularities leaves us with a smooth function I_ℓ on each interval of integration (possibly in terms of a new independent variable). The functions $F_\ell^{(1)}(a)$ and $F_\ell^{(2)}(a)$ are thus given by sums of integrals of smooth functions over a number of intervals. In what follows, we describe the integration over a *single* interval for which no change of variables is required. The extension to the fully general setting, with multiple integration intervals and changes of variables, is straightforward.

Thus, given the smooth function $I_\ell(r)$ on the integration interval $[\alpha, \beta]$, we seek to compute the functions

$$G_\ell^{(1)}(a) = \int_\alpha^a Y_\ell(\kappa a) J_\ell(\kappa r) I_\ell(r) r \, \mathrm{d}r, \tag{17}$$

$$G_\ell^{(2)}(a) = \int_a^\beta J_\ell(\kappa a) Y_\ell(\kappa r) I_\ell(r) r \, \mathrm{d}r. \tag{18}$$

3.1. Chebyshev approximation

To do this, we approximate $I_\ell(r)$ by means of a polynomial expansion of order N_c on each one of N_i equally sized subintervals $\mathscr{I}_k$ of $[\alpha, \beta]$

$$I_\ell(r) \approx \sum_{n=0}^{N_\mathrm{c}-1} c_{nk\ell} p_{nk}(r) \quad \text{for } r \in \mathscr{I}_k, k = 1, \ldots, N_\mathrm{i}. \tag{19}$$

Here $c_{nk\ell}$ are complex-valued coefficients, p_{nk} is a polynomial of degree n, and $\mathscr{I}_k = [a_{k-1}, a_k]$, where, calling $h = (\beta - \alpha)/N_\mathrm{i}$, we have set $a_k = \alpha + kh$.

There are several possible choices for the expansion polynomials $p_{nk}(r)$. In [1,2], Lagrange interpolating polynomials are used. However, for Lagrange polynomials, the computation of the coefficients $c_{nk\ell}$ is numerically unstable for large N_c [16, pp. 113–116]. In [1,2], the authors reduce this instability somewhat through use of a more stable, albeit computationally more expensive, algorithm, requiring $\mathscr{O}(N_\mathrm{c}^3)$ operations on each subinterval (see also [16, pp. 113–116]).

Chebyshev polynomials T_n, on the other hand, possess excellent approximation properties (closely approximating the minimax polynomial [17, pp. 225–236]) while also allowing stable evaluation of the $c_{nk\ell}$ in $\mathscr{O}(N_\mathrm{c}^2)$ operations (which can be further reduced to $\mathscr{O}(N_\mathrm{c} \log N_\mathrm{c})$ through use of FFTs [16, p. 187]). Using Chebyshev polynomials, then, for $r \in \mathscr{I}_k$, we have

$$I_\ell(r) \approx \sum_{n=0}^{N_\mathrm{c}-1} c_{nk\ell} T_n(x_k(r)), \tag{20}$$

where the function $x_k(r) = h^{-1}[2r - (a_{k-1} + a_k)]$ is simply a linear map from $\mathscr{I}_k$ to the standard Chebyshev interval $[-1, 1]$.

The evaluation of the Chebyshev coefficients for a function defined on $[-1, 1]$ requires the function values at the points

$$y_j = \cos\left(\frac{\pi(j - 1/2)}{N_\mathrm{c}}\right) \tag{21}$$

for $j = 1, \ldots, N_c$. Hence, we require the value of $I_\ell(r)$ at the points $a_{jk} = x_k^{-1}(y_j)$ for $j = 1, \ldots, N_\mathrm{c}$ and $k = 1, \ldots, N_\mathrm{i}$. These a_{jk} do not include the endpoints of the subintervals (since the y_j do not include the endpoints of $[-1, 1]$). However, as we will need these endpoints for parts of our calculation, we define $a_{0k} = a_{k-1}$ and $a_{N_\mathrm{p}k} = a_k$ for $k = 1, \ldots, N_\mathrm{i}$, where $N_\mathrm{p} = N_\mathrm{c} + 1$.

Since in our algorithm the order N_p of the Chebyshev approximation is held fixed, evaluation of the coefficients c_{nkl} for $n = 0, \ldots, N_c - 1$, $k = 1, \ldots, N_i$ and $\ell = -M, \ldots, M$ requires a total of $\mathcal{O}(N_p N_i M) = \mathcal{O}(N)$ memory and $\mathcal{O}(N_i M N_p^2) = \mathcal{O}(N)$ operations. As noted earlier, the N_p^2 complexity required by the Chebyshev approximation could be reduced to $\mathcal{O}(N_p \log N_p)$ by use of FFTs. Note that, since N_p remains fixed, however, a recourse to FFTs does not improve the overall asymptotic complexity. And, more importantly, since we typically use a relatively small value of N_p, e.g., $N_p = 9, 17$, we have found that use of FFTs in this context provides little additional benefit.

3.2. High-order radial integration

As we show in what follows, given the Chebyshev approximations of I_ℓ on each subinterval $\mathcal{I}_k$ of $[\alpha, \beta]$, the integrals (17) and (18) can be evaluated in terms of the integral moments

$$P_{njk\ell} = \int_{a_{0k}}^{a_{jk}} J_\ell(\kappa r) T_n(x_k(r)) r \, \mathrm{d}r \tag{22}$$

and

$$Q_{njk\ell} = \begin{cases} \int_{a_{jk}}^{a_{N_p k}} Y_\ell^{\mathrm{polar}}(\kappa r) T_n(x_k(r)) r \, \mathrm{d}r & \text{if } \alpha = 0, \\ \int_{a_{jk}}^{a_{N_p k}} Y_\ell(\kappa r) T_n(x_k(r)) r \, \mathrm{d}r & \text{if } \alpha > 0, \end{cases} \tag{23}$$

where

$$Y_\ell^{\mathrm{polar}}(z) = Y_\ell(z) - \frac{2}{\pi} \log\left(\frac{z}{2}\right) J_\ell(z)$$

is the part of the Neumann function Y_ℓ which contains singularities of the type $r^{-\ell}$ at the origin. The computation of these moments is non-trivial, in part, because of the rapid decay of J_ℓ for large ℓ near the origin as well as the polar singularities in Y_ℓ at the origin. As shown in Appendix B, however, these moments, which need only be computed once at the beginning of each run, can be obtained with the needed accuracy in $\mathcal{O}(N)$ operations and they require $\mathcal{O}(N)$ units of memory.

(The subtraction of the logarithmic term in the definitions of the moments $Q_{njk\ell}$ for $\alpha = 0$ eliminates the only *actual* singularity in the integrand of (18) – note that, since $G_\ell^{(2)}(0) = 0$ for $\ell \geqslant 1$, the $r^{-\ell}$ terms only give rise to *near*-singularities, which can be resolved by Gaussian integrations as described in Appendix B. The logarithmic singularity can be resolved through integration by parts treated as described below.)

To evaluate the integrals (17) and (18) we proceed as follows:

(1) We use the moments $P_{njk\ell}$ and $Q_{njk\ell}$ to obtain the integrals

$$A_{jk\ell} = \int_{a_{0k}}^{a_{jk}} J_\ell(\kappa r) I_\ell(r) r \, \mathrm{d}r,$$
$$B_{jk\ell} = \int_{a_{jk}}^{a_{N_p k}} Y_\ell(\kappa r) I_\ell(r) r \, \mathrm{d}r.$$

(2) We use $A_{jk\ell}$ and $B_{jk\ell}$ to obtain the integrals (17) and (18)

$$\begin{aligned} G_\ell^{(1)}(a_{jk}) &= Y_\ell(\kappa a_{jk}) \left(A_{jk\ell} + \sum_{q=1}^{k-1} A_{N_p q \ell} \right), \\ G_\ell^{(2)}(a_{jk}) &= J_\ell(\kappa a_{jk}) \left(B_{jk\ell} + \sum_{q=k+1}^{N_i} B_{0q\ell} \right). \end{aligned} \tag{24}$$

Remark 3. The quantities $A_{jk\ell}$ can be obtained directly from the $P_{njk\ell}$:

$$A_{jk\ell} \approx Y_\ell(\kappa a_{jk}) \sum_{n=0}^{N_c-1} c_{nk\ell} P_{njk\ell}.$$

Similarly, for $\alpha > 0$, the $B_{jk\ell}$ are obtained directly from the $Q_{njk\ell}$:

$$B_{jk\ell} \approx J_\ell(\kappa a_{jk}) \sum_{n=0}^{N_c-1} c_{nk\ell} Q_{njk\ell}.$$

Our method for the evaluation of $G_\ell^{(2)}(a_{jk})$ in the case $\alpha = 0$, which is less direct, is described below.

Remark 4. In practice, for large values of ℓ, the function J_ℓ (resp. Y_ℓ) may underflow (resp. overflow) causing the quantities $A_{jk\ell}$ (resp. $B_{jk\ell}$) in point (1) above, in turn, to underflow (resp. overflow). To overcome this difficulty, for sufficiently large values of the ratio $\ell/(\kappa a_{jk})$, we redefine $A_{jk\ell}$, $B_{jk\ell}$, $P_{njk\ell}$ and $Q_{njk\ell}$, e.g.,

$$\begin{aligned} A_{jk\ell} &= \int_{a_{0k}}^{a_{jk}} Y_\ell(\kappa a_{jk}) J_\ell(\kappa r) I_\ell(r) r \, \mathrm{d}r, \\ P_{njk\ell} &= \int_{a_{0k}}^{a_{jk}} Y_\ell(\kappa a_{jk}) J_\ell(\kappa r) T_n(x_k(r)) r \, \mathrm{d}r, \end{aligned} \tag{25}$$

with analogous redefinitions of $B_{jk\ell}$ and $Q_{njk\ell}$, and corresponding changes to (24). It is easy to check that, in view of the asymptotic properties of J_ℓ and Y_ℓ, the quantities (25) do not underflow or overflow. A method for the evaluation of products of the form $J_\ell(z_1)Y_\ell(z_2)$ that are needed in (25) is presented in Section 4.

As mentioned in Remark 3, it remains for us to evaluate $G_\ell^{(2)}(a_{jk})$ in the case $\alpha = 0$. In view of the relation

$$B_{jk\ell} \approx \int_{a_{jk}}^{a_{N_p k}} \frac{2}{\pi} \log\left(\frac{\kappa r}{2}\right) J_\ell(\kappa r) I_\ell(r) r \, \mathrm{d}r + \sum_{n=0}^{N_c-1} c_{nk\ell} Q_{njk\ell},$$

to do this it suffices to evaluate integrals of the form

$$\int_a^\beta \frac{2}{\pi} \log\left(\frac{\kappa r}{2}\right) J_\ell(\kappa r) I_\ell(r) r \, \mathrm{d}r \tag{26}$$

for all relevant values of ℓ and $a \in [\alpha, \beta] = [0, \beta]$.

To evaluate the integrals (26), we integrate the logarithmic term by parts to obtain

$$\begin{aligned} \int_a^\beta \log\left(\frac{\kappa r}{2}\right) J_\ell(\kappa r) I_\ell(r) r \, \mathrm{d}r &= \log\left(\frac{\kappa r}{2}\right) \int_0^r J_\ell(\kappa\rho) I_\ell(\rho) \rho \, \mathrm{d}\rho \Big|_a^\beta - \int_a^\beta \mathrm{d}r \frac{1}{r} \int_0^r J_\ell(\kappa\rho) I_\ell(\rho) \rho \, \mathrm{d}\rho \\ &= \log\left(\frac{\kappa\beta}{2}\right) G_\ell^{(1)}(\beta) - \log\left(\frac{\kappa a}{2}\right) G_\ell^{(1)}(a) - \int_a^\beta r^{-1} G_\ell^{(1)}(r) \, \mathrm{d}r. \end{aligned} \tag{27}$$

Since $r^{-1}G_\ell^{(1)}(r)$ is smooth for $r \geqslant 0$ ($G_\ell^{(1)}(r) = \mathcal{O}(r)$ as $r \to 0$), the last term in (27) can be computed by means of the high-order Chebyshev approximation

$$r^{-1} G_\ell^{(1)}(r) \approx \sum_{n=0}^{N_c-1} d_{nk\ell} T_n(x_k(r)) \quad \text{for } r \in \mathscr{I}_k.$$

The evaluation of the coefficients $d_{nk\ell}$ requires the values of $G_\ell^{(1)}(a_{jk})$, which have been obtained previously.

As is known, the Chebyshev coefficients of an indefinite integral can be obtained easily from the coefficients of the integrand [16, pp. 189, 190]; in our case, the Chebyshev coefficients $D_{nk\ell}$ of the antiderivative of $r^{-1}G_\ell^{(1)}(r)\,\mathrm{d}r$ are given by

$$D_{nk\ell} = \frac{d_{n-1k\ell} - d_{n+1k\ell}}{2n}, \quad n \geqslant 1.$$

The constant of integration $D_{0k\ell}$ is arbitrary. Clearly, this mapping requires only $\mathcal{O}(N)$ operations.

In summary, given accurate values of the integral moments $P_{njk\ell}$ and $Q_{njk\ell}$, the Chebyshev-based radial integration method presented in this section evaluates the integrals (8) with high-order accuracy in $\mathcal{O}(N)$ operations. This algorithm is significantly more efficient and stable than the Lagrange polynomial approach used in [1,2].

4. Accurate and efficient computation of scaled Bessel functions

As explained in Section 3, the rapid decay of the Bessel functions $J_\ell(z)$ and the rapid growth of the Neumann functions $Y_\ell(z)$ as ℓ increases gives rise to quantities that underflow and overflow, respectively, but whose product is machine-representable. To address these and other related issues we introduce certain scaled versions of J_ℓ and Y_ℓ.

Noting that the leading order asymptotics of the functions $J_\ell(z)$ and $Y_\ell(z)$ near the origin are given by

$$J_\ell(z) \sim \frac{1}{\ell!}\left(\frac{z}{2}\right)^\ell, \tag{28}$$

$$Y_\ell(z) \sim -\frac{(\ell-1)!}{\pi}\left(\frac{z}{2}\right)^{-\ell} \tag{29}$$

for integers $\ell > 0$ we introduce the scaled Bessel functions

$$\tilde{J}_\ell(z) = \ell!\left(\frac{z}{2}\right)^{-\ell} J_\ell(z), \tag{30}$$

$$\tilde{Y}_\ell(z) = -\frac{\pi}{(\ell-1)!}\left(\frac{z}{2}\right)^{\ell} Y_\ell(z). \tag{31}$$

These scaled Bessel functions can be used to compute needed products and quotients of J_ℓ and Y_ℓ. For example, we can compute the product $J_\ell(z_1)Y_\ell(z_2)$ for integers $\ell > 0$ as

$$J_\ell(z_1)Y_\ell(z_2) = -\frac{1}{\pi\ell}\left(\frac{z_1}{z_2}\right)^\ell \tilde{J}_\ell(z_1)\tilde{Y}_\ell(z_2). \tag{32}$$

These scaled Bessel functions can be evaluated by recurrence-relation techniques similar to those used to compute the conventional Bessel functions [16, pp. 173–175]. Indeed, from (30) and (31), and using the recurrence relations for J_ℓ and Y_ℓ, we obtain the recurrence relations

$$\tilde{J}_{\ell+1}(z) = \ell(\ell+1)\left(\frac{2}{z}\right)^2\left[\tilde{J}_\ell(z) - \tilde{J}_{\ell-1}(z)\right], \tag{33}$$

$$\tilde{Y}_{\ell+1}(z) = \tilde{Y}_\ell(z) - \frac{1}{\ell(\ell+1)}\left(\frac{z}{2}\right)^2 \tilde{Y}_{\ell-1}. \tag{34}$$

Numerical experiments clearly demonstrate that, as is the case for the recurrence relation associated with $J_\ell(z)$ and $Y_\ell(z)$, for increasing ℓ the recurrence for $\tilde{J}_\ell$ is unstable and the recurrence for $\tilde{Y}_\ell$ is stable. Our procedure for evaluation of the scaled Bessel functions thus proceeds as follows: we first use the classical algorithms to compute $Y_0(z)$ and $Y_1(z)$, we scale these values, and we then use the recurrence relation (34) to compute $\tilde{Y}_\ell(z)$. To compute $\tilde{J}_\ell(z)$, we use a downward recurrence and the normalization sum

$$1 = J_0(z) + 2\sum_{n=1}^{\infty} J_{2n}(z).$$

The implementation of this algorithm involves only relatively simple modifications to an existing recursive algorithm for evaluation of the Bessel functions $J_\ell(z)$ or $Y_\ell(z)$. In our codes, we used modified versions of the Fortran77 routines *rjbesl* and *rybesl*, provided in the Netlib repository [18].

5. Efficient preconditioning

Sections 2 and 3 describe our integration method for the evaluation of the function $K^M v^M$ for a given function

$$v^M(a,\phi) = \sum_{\ell=-M}^{M} v_\ell(a)\mathrm{e}^{\mathrm{i}\ell\phi}.$$

For a given inhomogeneity and a given discretization, that method can be used to produce matrix–vector products for the matrix associated with the linear system

$$v_\ell(a_{jk}) - (K_\ell v^M)(a_{jk}) = u^{\mathrm{i}}_\ell(a_{jk}), \quad \ell = -M,\ldots,M, \tag{35}$$

see Eq. (5). Clearly, this matrix–vector multiplication algorithm can be combined with any suitable iterative linear solver to yield a fast, high-order solver for our scattering problem. For the non-Hermitian linear systems arising in our context one may, in principle, use solvers such as GMRES, CGS, BiCGSTAB and QMR [19]. We have found, however, that only GMRES and BiCGSTAB performed consistently well for our problem; see e.g. [19] for a discussion of convergence rates of iterative linear solvers.

As is known, for a finite-dimensional linear system arising from discretization of a second-kind integral equation, the number of iterations required by an iterative solver to obtain a given residual tolerance *does not* depend on the mesh size. The number of iterations needed to meet a given tolerance does depend markedly on the size of the scatterer, however: for a given scattering geometry, as the frequency and/or the values of m are increased, the number of iterations required to achieve a given residual tolerance can increase considerably.

In this section, we introduce a preconditioning method which, based on use of approximate scatterers and associated preconditioning matrices P, can reduce significantly the number of iterations required by iterative solvers in our context. To construct a preconditioner we begin by approximating a given inhomogeneity m by a piecewise-constant, radially layered inhomogeneity $\widetilde{m}$; a preconditioner is then obtained as the inverse of an integral operator associated with $\widetilde{m}$ which, using a certain differential equation together with radial integration methods similar to those described in the previous sections, can be applied in $\mathcal{O}(N)$ operations. (The solution to this preconditioning integral operator bears some similarities to the well-known Mie series solution for scattering by a piecewise-constant layered cylinder; see Remark 5 for more details.)

To complete our preconditioning prescriptions we must make appropriate choices of the approximating inhomogeneities $\widetilde{m}$. In Section 5.2 we determine an approximating scatterer $\widetilde{m}$ for a given scatterer m which,

according to our extensive numerical experiments, is optimal: for a large class of scattering obstacles, including all of the test cases considered in Section 6, the $\widetilde{m}$ functions introduced in Section 6 provide the sharpest decreases in iteration numbers amongst those arising from admissible approximating scatterers.

5.1. Evaluation of the preconditioning operator

As mentioned above, we use functions $\widetilde{m}$ of the form

$$\widetilde{m}(x) = \sum_{j=1}^{q} m_j \chi_{A_j}(x),$$

where m_j are constants, χ_{A_j} is the characteristic function of the set A_j, and where A_j ($j = 1, 2, \ldots, q$) denote the annular sets

$$A_j = \{x : a_{j-1} \leqslant |x| \leqslant a_j\}, \quad 0 = a_0 < a_1 < \cdots < a_q = R_1.$$

Here we have assumed that $R_0 = 0$ for definiteness; the case for $R_0 > 0$ can be treated similarly – the slight departures in treatment that occur in this case will be pointed out at appropriate points in the text. The preconditioner P we use equals the *inverse* of the matrix associated with the integral equation

$$v(x) + \kappa^2 \sum_{j=1}^{q} m_j \int_{A_j} \Phi(\kappa|x-y|) v(y)\, \mathrm{d}y = \omega(x), \tag{36}$$

where, for convenience, the Green function g is expressed explicitly in terms of the Hankel function $\Phi(z) = (\mathrm{i}/4) H_0^1(z)$. Given the inverse operator P, our left-preconditioned equation reads

$$P(I - K^M) v^M = P u^{\mathrm{i},M}.$$

This new, preconditioned linear system is solved using an iterative solver, as described previously. In detail, after evaluating the right-hand side vector $P u^{\mathrm{i},M}$ by solving Eq. (36) with $\omega = u^{\mathrm{i},M}$, at each iteration of the linear solver, we solve (36) with $\omega = (I - K^M) v^M$ for the function v^M produced by the previous iteration of the iterative solver. Note that in both cases we have $\omega = \omega^M$.

To solve Eq. (36) for a given right-hand side ω we derive a differential equation for the new unknown $\mu = v - \omega$, where v is the solution of Eq. (36). Although v is only defined for $|x| \leqslant R_1$, we can extend μ to all of $\mathbb{R}^2$ by

$$\mu(x) = -\kappa^2 \sum_{j=1}^{q} m_j \int_{A_j} \Phi(\kappa|x-y|) v(y)\, \mathrm{d}y.$$

Clearly, for $x \in A_j$, we have

$$(\Delta + \kappa^2 n_j^2) \mu(x) = \kappa^2 m_j \omega, \quad j = 1, 2, \ldots, q, \tag{37}$$

where $m_j = 1 - n_j^2$ and for $|x| > R_1$ (and $|x| < R_0$ when $R_0 \neq 0$), we have

$$(\Delta + \kappa^2) \mu(x) = 0. \tag{38}$$

Further, $\mu \in C^1(\mathbb{R}^2)$ [20, pp. 53, 56] and, as it is easily seen, μ satisfies the Sommerfeld radiation condition as $|x| \to \infty$ [7, pp. 216–217]. Thus, Eqs. (37) and (38) together with the Sommerfeld radiation condition and conditions of continuity of the function μ and its radial derivatives at $|x| = a_j$ ($j = 0, \ldots, q$) make up a differential equation for μ in all of $\mathbb{R}^2$ that is equivalent to the preconditioning integral equation (36).

To solve this differential equation we express the solution as a sum of a particular solution and a solution of the associated homogeneous problem, $\mu(x) = \mu_{\mathrm{p}}(x) + \mu_{\mathrm{h}}(x)$. For $x \in A_j$, a particular solution to the equation is given by

$$\mu_{\mathrm{p}}(x) = -\kappa^2 m_j \int_{A_j} \Phi(\kappa n_j |x-y|)\omega(y)\,\mathrm{d}y.$$

Since $\omega = \omega^M$, it follows that $\mu_{\mathrm{p}} = \mu_{\mathrm{p}}^M$ and, further, in polar coordinates (a,ϕ), we have

$$(\mu_{\mathrm{p}})_\ell(a) = -\kappa^2 m_j \left[H_\ell^1(\kappa n_j a) \int_{a_{j-1}}^{a} J_\ell(\kappa n_j r)\omega_\ell(r) r\,\mathrm{d}r + J_\ell(\kappa n_j a) \int_a^{a_j} H_\ell^1(\kappa n_j r)\omega_\ell(r) r\,\mathrm{d}r \right] \tag{39}$$

for $a_{j-1} \leqslant a \leqslant a_j$. Clearly, these integrals can be computed with high-order accuracy and in $\mathcal{O}(N)$ operations using the radial integration method introduced in Section 3. Since this integration algorithm requires the values of $\omega_\ell(r)$ at Chebyshev points, we choose the preconditioning intervals $[a_{j-1}, a_j]$ to correspond to the radial integration intervals used to compute $\omega^M = (I - K^M)v^M$, so that interpolations are not needed to obtain the required values of $\omega_\ell(r)$.

The solution of the homogeneous problem, on the other hand, can be expressed in the form

$$\mu_{\mathrm{h}}(a,\phi) = \begin{cases} \sum_{\ell=-\infty}^{\infty} \alpha_\ell^{(1)} J_\ell(\kappa n_j a)\mathrm{e}^{\mathrm{i}\ell\phi} & \text{if } j = 1, \\ \sum_{\ell=-\infty}^{\infty} \left[\alpha_\ell^{(j)} J_\ell(\kappa n_j a) + \beta_\ell^{(j-1)} Y_\ell(\kappa n_j a) \right] \mathrm{e}^{\mathrm{i}\ell\phi} & \text{if } j = 2,3,\ldots,q \end{cases} \tag{40}$$

for $a_{j-1} \leqslant a \leqslant a_j$. (If $R_0 > 0$, the solution of the homogeneous problem for $j = 1$ is given by a linear combination of J_ℓ and Y_ℓ instead of J_ℓ alone. Furthermore, if $R_0 > 0$, we must consider the solution of the homogeneous problem in the additional region $a < R_0$, which takes the same form as for $j = 1$ in (40).) Finally, for $a > R_1$, we have

$$\mu(a,\phi) = \sum_{\ell=-\infty}^{\infty} \beta_\ell^{(q)} H_\ell^1(\kappa a)\mathrm{e}^{\mathrm{i}\ell\phi}.$$

Clearly, given the correct values of the coefficients $\alpha_\ell^{(j)}$ and $\beta_\ell^{(j)}$, we can compute $(\mu_{\mathrm{h}})_\ell(a)$ for $\ell = -M,\ldots,M$ and all radial discretization points in $\mathcal{O}(N)$ operations.

Remark 5. Our preconditioner is related to the Mie series solution of (1) for a layered cylinder with a piecewise-constant refractive index. Indeed, the form of the solution μ_{h} of the homogeneous problem exactly matches that of the Mie series solution. However, unlike the Mie solution, the inhomogeneous equation (37) requires a particular solution μ_{p} in addition to μ_{h}, which, in turn, affects the coefficients in the series expansion of μ_{h} through the continuity conditions on the boundaries between the annular regions.

Equations determining the values of the $2q$ coefficients $\alpha_\ell^{(j)}$ and $\beta_\ell^{(j)}$ are obtained by enforcing the conditions mentioned above, of continuity of μ and its radial derivatives at the points a_j, $j = 1,2,\ldots,q$. For $j = 2,3,\ldots,q-1$, we have

$$\alpha_\ell^{(j)} J_\ell(\kappa n_j a_j) + \beta_\ell^{(j-1)} Y_\ell(\kappa n_j a_j) + (\mu_{\mathrm{p}})_\ell(a_j^-) = \alpha_\ell^{(j+1)} J_\ell(\kappa n_{j+1} a_j) + \beta_\ell^{(j)} Y_\ell(\kappa n_{j+1} a_j) + (\mu_{\mathrm{p}})_\ell(a_j^+)$$

and

$$\begin{aligned} &\alpha_\ell^{(j)} n_j J_\ell'(\kappa n_j a_j) + \beta_\ell^{(j-1)} n_j Y_\ell'(\kappa n_j a_j) + \frac{1}{\kappa}(\mu_{\mathrm{p}})_\ell'(a_j^-) \\ &\quad = \alpha_\ell^{(j+1)} n_{j+1} J_\ell'(\kappa n_{j+1} a_j) + \beta_\ell^{(j)} n_{j+1} Y_\ell'(\kappa n_{j+1} a_j) + \frac{1}{\kappa}(\mu_{\mathrm{p}})_\ell'(a_j^+). \end{aligned}$$

Here $(\mu_p)_\ell(a_j^+) = \lim_{a\to a_j^+}(\mu_p)_\ell(a)$ and $(\mu_p)_\ell(a_j^-) = \lim_{a\to a_j^-}(\mu_p)_\ell(a)$ with corresponding definitions for the derivatives. The equations for $j = 1$ and $j = q$ are similar.

For each ℓ, the matrix associated with this linear system is constant and banded with five diagonals. Hence, we compute the LU-decomposition of all of these matrices in $\mathcal{O}(qM)$ operations [21, pp. 152, 153] only once at the beginning of each run. In each iteration, after computing the $(\mu_p)_\ell(a_j^+)$ and $(\mu_p)_\ell(a_j^-)$ and their derivatives, we use the LU-decomposition to solve for the values of $\alpha_\ell^{(j)}$ and $\beta_\ell^{(j)}$ for all $j = 1, 2, \ldots, q$. This again requires a total of $\mathcal{O}(qM)$ operations [21, pp. 152, 153].

Finally, we compute $(\mu_p)_\ell(a_j^+)$ and $(\mu_p)_\ell(a_j^-)$ and their derivatives. By (39), we have

$$(\mu_p)_\ell(a_{j-1}^+) = -\frac{i\pi}{2}\kappa^2 m_j J_\ell(\kappa n_j a_{j-1}) \int_{a_{j-1}}^{a_j} H_\ell^1(\kappa n_j r)\omega_\ell(r) r \, dr,$$

$$(\mu_p)_\ell(a_j^-) = -\frac{i\pi}{2}\kappa^2 m_j H_\ell^1(\kappa n_j a_j) \int_{a_{j-1}}^{a_j} J_\ell(\kappa n_j r)\omega_\ell(r) r \, dr$$

and

$$(\mu_p)'_\ell(a_{j-1}^+) = -\frac{i\pi}{2}\kappa^3 n_j m_j J'_\ell(\kappa n_j a_{j-1}) \int_{a_{j-1}}^{a_j} H_\ell^1(\kappa n_j r)\omega_\ell(r) r \, dr,$$

$$(\mu_p)'_\ell(a_j^-) = -\frac{i\pi}{2}\kappa^3 n_j m_j (H_\ell^1)'(\kappa n_j a_j) \int_{a_{j-1}}^{a_j} J_\ell(\kappa n_j r)\omega_\ell(r) r \, dr.$$

These integrals are easily obtained from the values of $(\mu_p)_\ell(a)$ in $\mathcal{O}(qM)$ operations.

This completes the description of the preconditioner resulting from a given approximating inhomogeneity $\widetilde{m}$; the constructions above show that such a preconditioner can be applied in just $\mathcal{O}(N)$ operations per iteration. A discussion on selection of the function $\widetilde{m}$ is given in the following section.

5.2. Optimal choice of preconditioning parameters

Naturally, the effectiveness of the preconditioner in reducing iteration numbers depends on the choice of the annuli A_j and the approximating indices m_j. A rather extensive set of numerical experiments we have conducted suggest the following strategy for the selection of these parameters: (1) use annuli A_j whose boundaries are tangent to curves of discontinuity in the actual index m; (2) use values m_j equal to the average value of m on the *outside* boundary of each A_j.

Following these rules, the optimal preconditioning parameters for the scatterers in Section 6.2 are as follows: (1) for the "bumpy" scatterer (Fig. 4) we use a single annulus A_1 (actually a disc in this case) covering the background disc and with $m_1 = -3$, the in-disc background index; (2) for the square-shaped scatterer (Fig. 2) and the star-shaped scatterer (Fig. 3), we use two preconditioning annuli, A_1 and A_2: A_1 is the inscribed disc and m_1 equals the value of m on that disc, which is a constant; the outer boundary of A_2 circumscribes the scatterer and $m_2 = 0$.

As demonstrated by the various tables in Section 6.2, with these prescriptions for the preconditioning parameters, the preconditioner introduced in this section can lead to very significant decreases in iteration numbers. The reductions that result from this preconditioner depend on the character of the given scattering geometry. To analyze the performance of the preconditioner as the scatterer geometry changes, we compared the number of iterations required to meet a given tolerance with and without preconditioning for elliptical scatterers of varying eccentricity. We used elliptical scatterers with constant refractive index $n = 2$ ($m = -3$), major axis of length equal to 10 interior wavelengths, and various minor axes. In accordance with our prescriptions above, the preconditioner contains two annuli, one inscribed with $m_1 = -3$ and one whose outer boundary circumscribes the ellipse, with $m_2 = 0$. As we varied the length of the minor axis

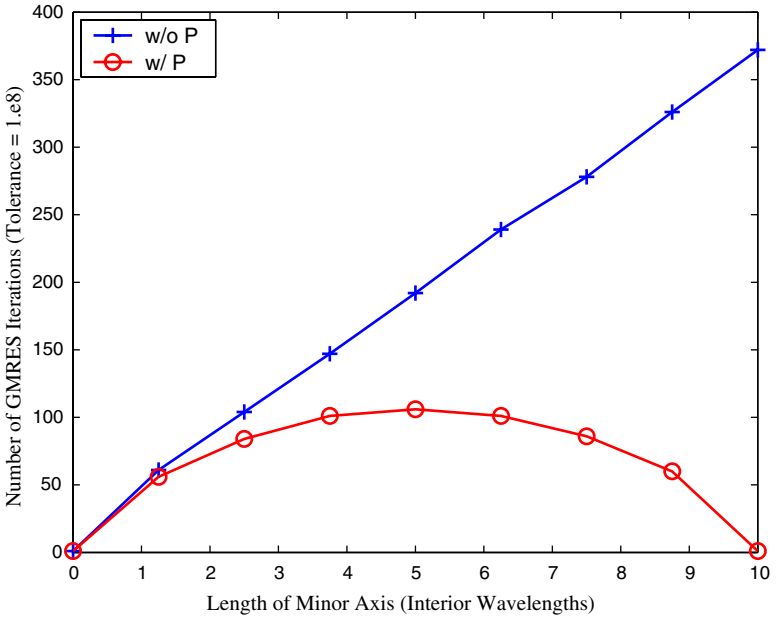

Fig. 1. Number of iterations for ellipses of varying minor axis length with and without preconditioning. Length of major axis = 10 interior wavelengths.

from 0 to 10 interior wavelengths, we recorded the number of GMRES iterations required to obtain a residual tolerance of 10^{-8} with and without preconditioning. The results of these experiments are displayed in Fig. 1.

We observe that, without preconditioning, the iteration number grows linearly from 1 to 372 as the minor axis increases from 0 to 10 wavelengths. With preconditioning, on the other hand, the number of iterations grows from 1 (when the minor axis is 0, i.e., the scatterer is empty) to a maximum of 106 (when the minor axis is 5) and then decreases back to 1 (when the minor axis is 10, i.e., for a circle). Hence, the relative decrease in the required number of iterations is least for thin ellipses, for which, clearly, there is comparatively little need for preconditioning *since so few iterations are required in such cases, even without preconditioning*.

Thus, the preconditioner is robust with respect to scatterer geometry: it provides the most significant benefits in problems for which the need is greatest.

6. Numerical results

In the following sections we demonstrate the character of our solver by means of a range of examples in a variety of scattering configurations. In Section 6.1 we study the convergence of the radial integration scheme described in Section 3 for both smooth and a discontinuous scatterers. In Section 6.2, we demonstrate the overall effectiveness of the method, including the preconditioner, for three rather complex scatterers containing inhomogeneities, discontinuities, corners and cusps. Finally, in Section 6.3, we demonstrate, in two numerical examples, the dramatic performance improvements our algorithm provides as compared with the approach originally proposed in [1,2].

In each example case, we report the maximum near field error ϵ_u^{nf} and/or the maximum far field error ϵ_u^{ff} for plane wave incidence, $u^{\mathrm{i}}(x,y) = \mathrm{e}^{\mathrm{i}\kappa x}$. To compute the maximum error in the near field, we interpolate the

solution computed by our method to an evenly spaced polar grid. On this grid, we compute the maximum absolute error as compared with either the analytical solution (when it is available) or the solution computed with a finer discretization. The maximum error in the far field is computed similarly by interpolating to an evenly spaced angular grid. The results for each example are given in the accompanying figures and tables. These results were obtained using the GMRES iterative solver on a 1.7 GHz Pentium Xeon.

6.1. Convergence of the radial integration algorithm

In this section, we demonstrate the high-order convergence of the radial integration method described in Section 3. (Of course, here and throughout the examples in this text we also make use of the scaled Bessel function algorithm described in Section 4.) The degree of accuracy in the radial integration is determined by the number of subintervals N_i and the number N_c of Chebyshev points per subinterval used to approximate $I_\ell(r)$ (see Appendix B for the parameters used in the evaluation of the integral moments (22) and (23)).

In each one of the following examples we present maximum near field errors for a fixed value of N_c, which determines the convergence order, as N_i is increased; see, for example, Table 1. For the examples in the present section we choose relatively small values of N_c, for which the convergence rates are easily

Table 1
Convergence of radial integration for a disc centered at the origin (diameter $= 2\sqrt{2}$ interior wavelengths)

N_i	M	ϵ_u^{nf}	Ratio
(a) $N_c = 2$			
4	15	0.760	
8	15	0.216	3.52
16	15	5.92e−2	3.65
32	15	1.42e−2	4.17
64	15	3.67e−3	3.87
128	15	9.36e−4	3.92
(b) $N_c = 3$			
4	15	9.77e−2	
8	15	1.24e−2	7.88
16	15	1.98e−3	6.26
32	15	3.83e−4	5.17
64	15	8.73e−5	4.39
128	15	2.05e−5	4.26
(c) $N_c = 4$			
4	15	1.15e−2	
8	15	8.25e−4	13.9
16	15	5.36e−5	15.4
32	30	3.49e−6	15.4
64	30	2.11e−7	16.5
128	30	1.37e−8	15.4
(d) $N_c = 5$			
4	15	1.19e−3	
8	15	4.61e−5	25.8
16	30	1.85e−6	24.9
32	30	9.69e−8	19.1
64	30	5.58e−9	17.4
128	30	3.28e−10	17.0

Table 2
Convergence of radial integration for a disc centered at $(1\lambda, 0)$ (diameter $= \sqrt{2}$ interior wavelengths)

N_i	M	ϵ_u^{nf}	Ratio
(*a*) $N_c = 2$ *without change of variable*			
1	15	2.34	
2	15	1.45	1.61
4	15	0.499	2.91
8	30	0.167	2.99
16	30	4.69e − 2	3.56
32	30	1.31e − 2	3.58
64	60	4.48e − 3	2.92
(*b*) $N_c = 2$ *with change of variable*			
1	15	2.93	
2	15	1.92	1.53
4	15	0.668	2.87
8	15	0.204	3.27
16	30	5.51e − 2	3.70
32	30	1.53e − 2	3.60
64	60	3.78e − 3	4.05
(*c*) $N_c = 4$ *without change of variable*			
1	7	1.52	
2	15	0.159	9.56
4	30	2.09e − 2	7.61
8	60	6.91e − 3	3.02
16	60	2.44e − 3	2.83
32	120	5.88e − 4	4.15
64	120	3.17e − 4	1.85
(*d*) $N_c = 4$ *with change of variable*			
1	15	1.82	
2	15	0.748	2.43
4	30	3.69e − 2	20.27
8	60	3.25e − 3	11.35
16	120	4.06e − 4	8.00
32	480	2.28e − 5	17.81
64	480	6.98e − 6	3.27
(*e*) $N_c = 8$ *without change of variable*			
1	30	2.60e − 2	
2	30	6.82e − 3	3.81
4	60	2.39e − 3	2.85
8	120	7.01e − 4	3.41
16	120	3.11e − 4	2.25
32	240	1.14e − 4	2.73
64	480	2.41e − 5	4.73
(*f*) $N_c = 8$ *with change of variable*			
1	15	0.536	
2	30	1.17e − 2	45.81
4	60	1.23e − 3	9.51
8	240	1.78e − 4	6.91
16	480	4.61e − 5	3.86
32	960	3.86e − 6	11.94
64	1920	3.40e − 7	11.35

observed. In practice (in the following sections), we use significantly larger values of N_c, which are much more advantageous. In each table, we also report the number of modes M used in the calculation. To ensure that the near field errors reported reflect the convergence rate of the radial integration scheme alone, in Tables 1 and 2 sufficiently large values of M were used so that the angular integration error is smaller than the radial integration error.

We demonstrate the radial convergence rates in two examples for which exact solutions are known: (1) a disc with constant refractive index centered at the origin, and (2) a disc with constant refractive index centered away from the origin. Although these scatterers are similar from a physical point of view, they present significantly different degrees of difficulty to our numerical algorithm. In particular, the disc centered at the origin gives rise to a smooth (constant) refractive index function within the integration domain whereas the disc centered away from the origin $n(x)$ is discontinuous in the integration domain. As described previously, a discontinuous refractive index requires special treatment: (1) a change of variables is required to resolve associated square-root singularities (see Section 3 and Appendix A), and (2) substitution by a truncated Fourier series m^{2M} is used (see Section 2).

In Table 1 we present results for the disc of diameter 2λ centered at the origin with refractive index $n = \sqrt{2}$, where λ is the wavelength of the incident field. Since, as it is apparent from these results, our radial integration method converges as $N_i^{-N_c}$ if N_c is even and as $N_i^{-(N_c-1)}$ if N_c is odd (a behavior similar to that exhibited by the Newton–Cotes quadrature rules [17, p. 264]), in practice, we only use even values of N_c. The value of N_c should be selected to balance convergence order and computational cost (the computation of the radial integrals requires $\mathcal{O}(N_c^2 N_i M) = \mathcal{O}(N_c N)$ operations); in our experience, we have found that the choice $N_c = 16$ strikes this balance quite well.

Results for the disc centered at $(1\lambda, 0)$ are given in Table 2. In this case, the disc has a diameter of 1λ and a refractive index of $n = \sqrt{2}$. We display the near and far field errors obtained with and without the change of variables, which resolves the square-root singularities in $I_\ell(r)$ (see Appendix A). We only present results for even values of N_c. We see that significant improvements in the convergence rate result when the change of variables is used.

Remark 6. From Tables 1 and 2, we observe that the number of Fourier modes M required to obtain a *high degree of accuracy* is much higher for the off-center disc than for the disc centered at the origin. (To obtain a low degree of accuracy, only small values of M are required in both cases.) This is a direct consequence of the fact, emphasized previously, that the index $m(r, \theta)$ for the off-center disc is a *discontinuous* function on the integration domain while the index for the disc centered at the origin is a C^∞ function on the integration domain. This difference in regularity gives rise to the difference in convergence rates that, in turn, is related to the differences in the values of M required for a given accuracy. As established in [13], the convergence rate of the algorithm under consideration for a discontinuous scatterer is $\mathcal{O}(M^{-2})$ in the near field and $\mathcal{O}(M^{-3})$ in the far field. The convergence rate for a C^∞ scatterer, on the other hand, is *superalgebraic* in M. Thus, we expect $\mathcal{O}(M^{-3})$ far field convergence for any discontinuous m; see, for example, the convergence behavior for the square-shaped scatterer in Table 3.

6.2. Complex scatterers and preconditioning

In this section, we demonstrate the capabilities of our method and the performance of our preconditioner by considering three rather complex scattering geometries. The first two of these scatterers contain geometric singularities, corners and cusps, respectively, as well as discontinuities in $n(x)$. The last example contains smooth indentations and protrusions in a constant background, providing an example of a truly inhomogeneous, smooth refractive index distribution. In each example, we present the maximum near and far field errors as we increase N_i and M while fixing $N_c = 16$. We choose the preconditioning parameters for each scatterer as described in Section 5.2. Furthermore, we report the number of GMRES iterations as well

Table 3
Convergence for the square-shaped scatterer (diagonal length = 10 interior wavelengths)

M	N_i	Memory (MB)		Iterations		Time (s)		ϵ_u^{nf}	ϵ_u^{ff}
		w/ P	w/o P	w/ P	w/o P	w/ P	w/o P		
60	2/2	13	33	52	218	8.56	23.0	6.15e − 2	4.32e − 2
120	2/3	31	79	56	226	21.4	60.8	1.22e − 2	3.60e − 3
240	2/5	90	228	58	235	61.8	181	1.70e − 3	3.21e − 4
480	2/10	311	795	62	238	218	623	4.25e − 4	3.64e − 5
960	2/20	1183		66		238		6.72e − 5	3.04e − 6

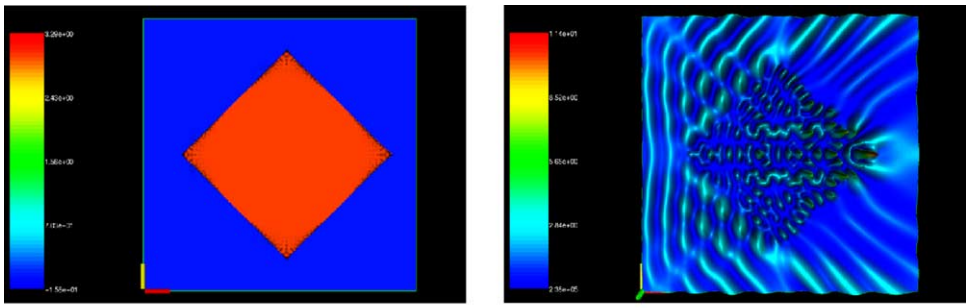

Fig. 2. Visualizations for the square-shaped scatterer. Diagonal length = 10 interior wavelengths: (a) scatterer ($q = -m = n^2 - 1$); (b) near field intensity ($|u|^2$).

as the memory and the time required with and without the use of our preconditioner, indicated by "w/P" and "w/o P", respectively.

The square-shaped scatterer with constant refractive index, depicted in Fig. 2, is, like the off-center disc considered in the previous section, an example of a discontinuous refractive index distribution; numerical results for this configuration are given in Table 3. The length of the diagonal is 5λ and $n = 2$, where, again, λ is the wavelength of the incident field. Hence, in terms of interior wavelengths, the square has a diagonal length of 10λ. Our approach requires no special treatment of the corners: our algorithm only uses the Fourier coefficients $m_\ell(r)$ of m for each radius r – which can be computed easily and accurately for general scatterers, by either analytical or numerical means.

To properly treat the singularities in $m_\ell(r)$ at the tangency points (see Section 3) we divide the integration interval into its two subintervals $[0, 5\sqrt{2}/4\lambda]$ and $[5\sqrt{2}/4\lambda, 5/2\lambda]$. In Table 3, we list the number of subintervals in each of these intervals (as $N_i^{(1)}/N_i^{(2)}$). On the first interval, m is constant and, as shown in Appendix A), the Fourier coefficients $m_\ell(r)$ have a square-root singularity at $r = 5\sqrt{2}/4\lambda$ from the right; hence, we use the change of variable (16) on this interval.

Note that the slight noise in the visualization of the refractive index in Fig. 2(a) is caused by the Gibbs phenomenon in summing the truncated Fourier series m^{2M}. (This noise can be observed in the visualizations of the other discontinuous scatterers as well.) We emphasize that, as discussed in Section 2, this approximation of m by m^{2M} *does not* degrade the solution accuracy, but instead *improves* it by allowing efficient and *exact* computation of the Fourier coefficients of $m(r,\theta)v^M(r,\theta)$. As in previous examples, we observe second-order convergence in the near field and third-order convergence in the far field, as predicted by the theoretical results in [13]. Note that both time and memory scale roughly linearly with the number of unknowns $N = \mathcal{O}(N_i N_c M)$.

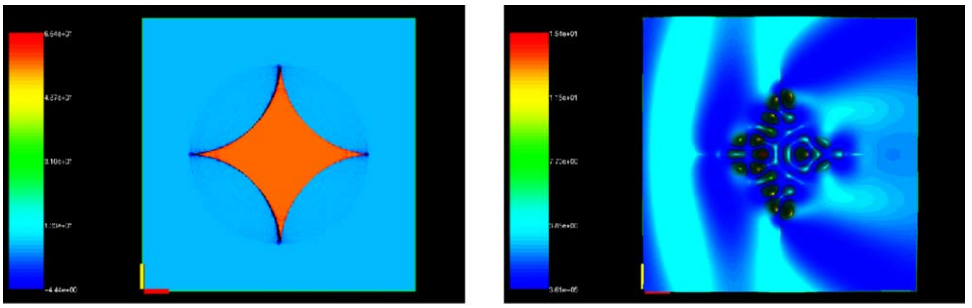

Fig. 3. Visualizations for the star-shaped scatterer. Diameter = 8 interior wavelengths: (a) scatterer ($q = -m = n^2 - 1$); (b) near field intensity ($|u|^2$).

The star-shaped scatterer depicted in Fig. 3(a) (which occupies the region between four unit discs centered at $(1,1)$, $(1,-1)$, $(-1,1)$ and $(-1,-1)$) contains cusps and, hence, would likely pose difficulties for most scattering solvers available. However, as with the square-shaped scatterer, no special treatment of such singularities is necessary within our approach. As in the previous examples, it suffices to evaluate the Fourier coefficients $m_\ell(r)$ which, in this case, can be obtained analytically. The wavenumber κ is chosen so that the scatterer has a diameter of 1λ, and for the refractive index we use $n = 8$. Hence, in terms of interior wavelengths, this scatterer measures 8λ in diameter.

As with the square-shaped scatterer, we divide the radial integration domain $[0, 1/2\lambda]$ into two intervals $[0, (\sqrt{2}-1)/2\lambda]$ and $[(\sqrt{2}-1)/2\lambda, 1/2\lambda]$. We again use the change of variables (16) to resolve the square-root singularity at the left endpoint of the second interval. In Table 4, we report the number of subintervals in each of these intervals as $N_{\mathrm{i}}^{(1)}/N_{\mathrm{i}}^{(2)}$.

The visualization of the near field intensity, Fig. 3(b), clearly shows the relatively long wavelength of the field outside the scatterer as well as the relatively short wavelength of the field inside the scatterer. Table 4 demonstrates the second-order convergence in the near field and third-order convergence in the far field. We also observe the proper scaling of the memory and time with M, N_{i} and the number of GMRES iterations. Indeed, for the finest discretization presented in Table 4, the computer used for the computations ran out of memory when using the unpreconditioned solver; hence, the last line of the table only reports data for the preconditioned solver.

The final example is given in Fig. 4. This scatterer was obtained by adding (or subtracting) several smooth "bumps" with randomly generated heights, radii and centers to a constant refractive index in a

Table 4
Convergence for the star-shaped scatterer (diameter = 8 interior wavelengths)

M	N_{i}	Memory (MB)		Iterations		Time (s)		ϵ_u^{nf}	ϵ_u^{ff}
		w/ P	w/o P	w/ P	w/o P	w/ P	w/o P		
30	1/2	6	6	32	73	3.16	3.46	0.792	0.581
60	1/4	14	15	35	77	7.76	8.95	0.112	9.34e − 2
120	1/6	36	42	37	80	19.5	23.7	2.02e − 2	1.28e − 2
240	1/10	113	143	40	82	61.3	72.7	3.87e − 3	1.65e − 3
480	1/18	403	543	43	85	219	261	9.01e − 4	2.06e − 4
960	1/34	1538		45		882		1.50e − 4	2.13e − 5

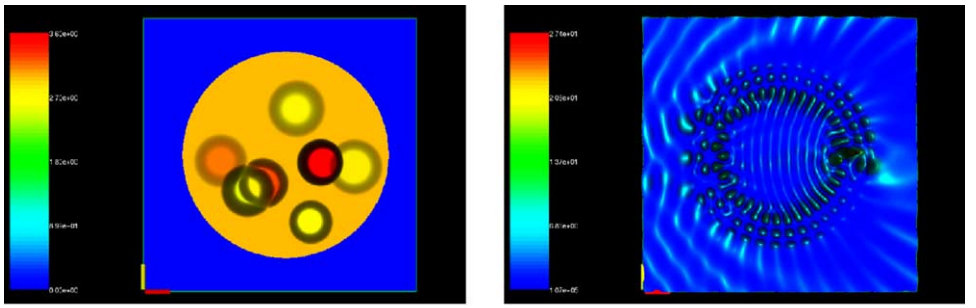

Fig. 4. Visualizations for the bumpy scatterer. Diameter ≈10 interior wavelengths: (a) scatterer ($q = -m = n^2 - 1$); (b) near field intensity ($|u|^2$).

disc. The disc-shaped background in this example has a diameter of 5λ and a refractive index $n = 2$ (interior wavelength diameter $= 10\lambda$). The bumps are simple smooth cylindrically symmetric functions given by

$$\phi(|x - x_0|) = \begin{cases} h, & |x - x_0| \leqslant t_0, \\ h \exp\left(\frac{2e^{-1/t}}{t-1}\right), & t_0 < |x - x_0| < t_1, \quad t = (|x - x_0| - t_0)/(t_1 - t_0), \\ 0, & |x - x_0| \geqslant t_1 \end{cases}$$

with randomly selected values of x_0, t_0, t_1 and h. Since this inhomogeneity is C^∞ in the integration domain, we need not resolve any singularities. As a result, unlike the previous example, we have only a single interval for the radial integration and we do not substitute m^{2M} for m, but rather compute $I_\ell(r)$ by means of direct trapezoidal rule integration with $N_\theta \approx 4M$ points (see Section 2). As expected, because of the smoothness of the inhomogeneity, we observe very rapid convergence in both the radial and angular integration (see Table 5).

In each example, we observe quite significant decreases in the required number of iterations when the preconditioner is used. Consistent with the discussion of Section 5.2 and the data in Fig. 1, we see the greatest decrease in the number of iterations for the scatterers whose unpreconditioned iteration count is highest. Finally, we point out that the comparison of memory requirements with and without preconditioning is most relevant when using (unrestarted) GMRES, as we did in these examples, since GMRES stores a new basis vector at each iteration; thus, the memory requirements are directly proportional to the number of iterations. If instead one uses a linear solver that does not store basis vectors, e.g., BiCGSTAB, the memory usage would not grow with the number of iterations; in this case, we would expect that the

Table 5
Convergence for the bumpy scatterer (diameter ≈10 interior wavelengths)

M	N_i	Memory (MB)		Iterations		Time (s)		ϵ_u^{nf}	ϵ_u^{ff}
		w/ P	w/o P	w/ P	w/o P	w/ P	w/o P		
30	3	5	27	12	439	1.38	21.6	1.38e − 2	5.32e − 3
60	7	14	107	15	445	5.69	120	2.22e − 4	3.41e − 5
120	12	47	368	20	457	22.5	426	5.24e − 6	3.46e − 7
240	26	221		23		131		7.50e − 8	2.83e − 10

memory with preconditioning to somewhat exceed the memory without preconditioning because of the storage requirements of the preconditioner itself.

6.3. Comparison with the original algorithm [1,2]

To compare the performance of the present method with that of the original algorithm [1,2] we consider two main examples. First, we compare the performance of our algorithm with that of the previous approach in a problem of scattering by a large disc with constant refractive index (compare Fig. 1 of [2]). Here we evaluate the maximum far field error for a disc centered at the origin with $n = \sqrt{2}$ for $\kappa R = 8$ and $\kappa R = 256$. The plotted curves in Fig. 5 are obtained by holding the number of subintervals N_i fixed (each value of N_i corresponds to one curve) and varying the degree $d = N_p - 1$ of the Chebyshev polynomials.

For $\kappa R \approx 10 - 15$, we observe very similar results for the two approaches; compare, for example, Fig. 5(a) below for $\kappa R = 8$ with the corresponding plot in Fig. 1 of [2]. However, the range $\kappa R \approx 10 - 15$ contains, roughly, the largest cylinders that the original approach could treat, owing to various inaccuracies and instabilities (e.g., inaccuracies in the moments calculations [see Appendix B], underflow/overflow errors in Bessel functions evaluations, etc.) as well as the lack of a preconditioner like the one we introduced in this text. The present algorithm, on the other hand, still delivers significant accuracy for $\kappa R = 256$, which is of the order of a 20 times larger (400 times larger in square wavelengths) than the largest problems that could be solved by means of the previous algorithm; see Fig. 5(b).

In our second example, we compare our algorithm's performance with that of the previous approach, as reported in [2], for the following smooth inhomogeneous scatterer:

$$m(x,y) = -0.15(1-x)^2 e^{-[x^2+(y+1)^2]} + 0.5\left(\frac{x}{5} - x^3 - y^5\right) e^{-(x^2+y^2)} + \frac{1}{60} e^{-[(x+1)^2+y^2]} \tag{41}$$

for $x^2 + y^2 \leqslant \pi^2$ and $m(x,y) = 0$ otherwise. In Table 6, we report maximum far field errors and computational times for both algorithms under an assumed incident field with $\kappa = 9$. (The results for the original approach were obtained from Table XI of [2].) Our algorithm ran on a 1.7 GHz PC and the original approach ran on a 400 MHz PC. Even taking into account the differences in computer hardware and software, our algorithm obviously far outperforms the original approach. We obtain, for example, an error of 8.9×10^{-13} in $2.12s$ compared with an error of 1.1×10^{-8} obtained in $88.91s$ by the original approach.

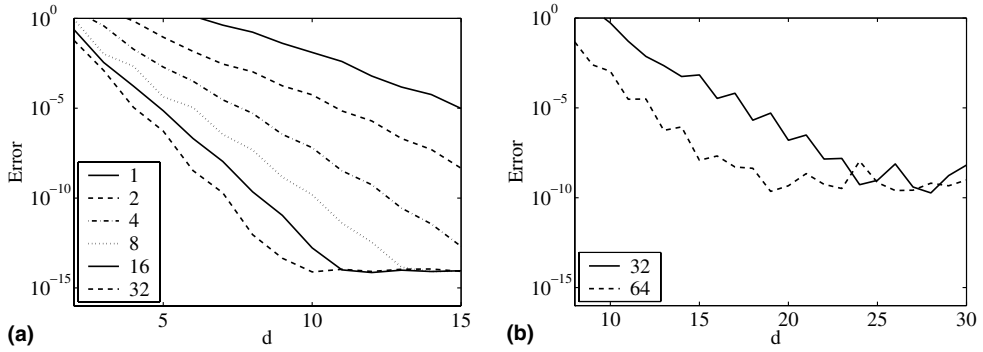

Fig. 5. Maximum far field errors for scattering by the disc $r \leqslant R$ as the degree $d = N_p - 1$ of the Chebyshev polynomials is increased for each of several values of N_i: (a) $\kappa R = 8$; (b) $\kappa R = 256$.

Table 6
Convergence for the smooth inhomogeneous scatterer (41) with $\kappa R = 9\pi$

M	N_r	Time (s)	Error
(*a*) *Current algorithm*			
28	27	0.10	8.9e − 2
32	34	0.20	1.2e − 3
34	51	0.32	8.7e − 5
36	51	0.37	5.2e − 6
38	68	0.56	2.4e − 7
40	85	0.82	8.2e − 9
45	153	2.12	8.9e − 13
(*b*) *Original algorithm*			
26	21	0.75	1.2e − 1
32	41	2.16	1.8e − 3
35	81	5.05	1.1e − 4
38	161	13.88	6.7e − 6
39	321	32.23	4.1e − 7
41	641	88.91	1.1e − 8

Acknowledgements

Color visualizations generated with the VTK-based visualization tool Vizamrai, developed by Steven Smith at the Center for Applied Scientific Computing (CASC), Lawrence Livermore National Laboratory.

Appendix A. Determination of the singularities in $m_\ell(r)$

As mentioned in Section 3, a point $r = r_0$ of tangency between polar circles and a discontinuity surface $\partial\mathscr{D}$ gives rise to a $|r - r_0|^\gamma$ singularity in the functions $m_\ell(r)$ and $I_\ell(r)$, for some γ with $0 < \gamma < 1$. These singularities must be resolved if high-order convergence in the radial integration algorithm is to be obtained. In particular, it is important to evaluate γ for a given tangency configuration; this can be done easily, as we show in what follows.

Consider the expression (A.1) for the Fourier coefficients $m_\ell(r)$. For r near the tangency radius r_0, the contribution to the Fourier coefficients $m_\ell(r)$ due to the set $\mathscr{D}$ is given by

$$m_\ell(r) = \frac{1}{2\pi}\int_{\alpha_1(r)}^{\alpha_2(r)} m(r,\theta)\mathrm{e}^{-\mathrm{i}\ell\theta}\,\mathrm{d}\theta, \tag{A.1}$$

where the quantities $\alpha_1(r)$ and $\alpha_2(r)$ give the polar coordinate angles at which the circle of radius r intersects $\partial\mathscr{D}$. Thus clearly, since $m(r,\theta)$ is smooth for $\alpha_1(r) \leqslant \theta \leqslant \alpha_2(r)$, the singularity in $m_\ell(r)$ is determined solely by the singularities in the functions $\alpha_2(r)$ and $\alpha_1(r)$ at $r = r_0$. The singularity in these functions, in turn, is determined by the nature of the tangency between the circle $r = r_0$ and $\partial\mathscr{D}$: a second-order tangency (in which the local behavior of $\partial\mathscr{D}$ relative to the circle $r = r_0$ is quadratic) gives rise to $\gamma = 1/2$ whereas an nth order tangency gives rise to $\gamma = 1/n$.

It follows that the off-center disc as well as the square- and star-shaped scatterers considered in Section 6 exhibit singularities with $\gamma = 1/2$. (These singularities are resolved by the change of variables (16).) For example, in the case of the off-center disc, we expect singularities of the type $[r - (d - R)]^{1/2}$ and $[(d + R) - r]^{1/2}$ at the tangency points $r = d - R$ and $r = d + R$, respectively. Explicit integration shows that the Fourier coefficients $m_\ell(r)$ for the off-center disc are given by

$$m_\ell(r) = \begin{cases} \frac{\bar{m}\alpha(r)}{\pi} & \text{if } \ell = 0, \\ \frac{\bar{m}\sin(\ell\alpha(r))}{\pi\ell} & \text{if } \ell \neq 0, \end{cases} \tag{A.2}$$

for $d - R \leqslant r \leqslant d + R$, where $\alpha_2(r) = -\alpha_1(r) = \alpha(r) = \arccos[(r^2 + (d^2 - R^2))/2dr]$ and $\bar{m} = 1 - n^2$. It is easy to verify that, as predicted by the analysis above, $\alpha(r)$ exhibits square-root singularities at $r = d - R$ and $r = d + R$.

Appendix B. Accurate evaluation of the integral moments

In this section, we present a method for accurate evaluation of the integral moments $P_{njk\ell}$ and $Q_{njk\ell}$. As noted in Section 3.1, the $r^{-\ell}$ growth of the functions Y_ℓ and the r^ℓ decay of the functions J_ℓ near the origin makes the development of accurate quadrature schemes for these moments a challenging problem: since quadrature rules typically depend on accurate polynomial interpolation, accurate integration of these functions would seem to require a large number of integration points for large values of ℓ.

In our context, however, accurate values for these moments are actually not difficult to obtain. The key insight is that since our goal is a small relative error in the value of the field v^M, it is sufficient to require that the individual Fourier coefficients of the field v_ℓ have an error that is small *relative to the total field* v^M. In particular, if a coefficient $v_\ell \ll v^M$, then v_ℓ contributes very little to the value – and hence, to the error – of v^M. More precisely, given a desired relative accuracy of ε in v^M , if we let δv_ℓ be the absolute error in the coefficient v_ℓ and let δv^M be the absolute error in v^M, then the necessary condition on δv_ℓ is

$$\frac{\delta v^M}{v^M} \leqslant \sum_{\ell=-M}^{M} \frac{\delta v_\ell}{v^M} < \varepsilon.$$

To compute these moments, we use Gaussian quadrature with N_g points to integrate between each pair of adjacent grid points a_{j-1k} and a_{jk} for $j = 1, \ldots, N_p$ and $k = 1, \ldots, N_i$. Gauss–Legendre integration of a function f defined on the interval $[a, b]$ is given by [17, pp. 276–279]

$$\int_a^b f(t)\,\mathrm{d}t \approx \left(\frac{b-a}{2}\right) \sum_{j=1}^{N_g} w_j f\left(\frac{b+a}{2} + \frac{b-a}{2} x_j\right), \tag{B.1}$$

where the points $-1 < x_j < 1$ are the zeroes in $[-1, 1]$ of the Legendre polynomial of degree N_g and $w_j > 0$ are the corresponding weights.

Our goal in this section is to show that, given a maximum error $\varepsilon > 0$ and an initial radial discretization, we can choose the number N_g in such a way that the error in the moment integrals is less that ε for all ℓ and for all subsequent refinements of the radial discretization.

By (28) and (29), for large ℓ, the moment integrals

$$P_\ell(a, b) = Y_\ell(\kappa b) \int_a^b J_\ell(\kappa r) T_n(x_k(r)) r\,\mathrm{d}r, \tag{B.2}$$

$$Q_\ell(a, b) = J_\ell(\kappa a) \int_a^b Y_\ell(\kappa r) T_n(x_k(r)) r\,\mathrm{d}r \tag{B.3}$$

have the same properties as

$$-\frac{1}{\pi\ell b^{\ell}}\int_a^b r^{\ell+1}\,\mathrm{d}r = -\frac{a^2}{\pi\ell(\ell+2)}\left[\left(\frac{b}{a}\right)^2-\left(\frac{a}{b}\right)^{\ell}\right], \tag{B.4}$$

$$\frac{a^{\ell}}{\pi\ell}\int_a^b r^{-\ell+1}\,\mathrm{d}r = -\frac{b^2}{\pi\ell(\ell-2)}\left[\left(\frac{a}{b}\right)^2-\left(\frac{a}{b}\right)^{\ell}\right], \tag{B.5}$$

respectively, where a and b are adjacent grid points. Thus, by considering the relatively simple quantities (B.4) and (B.5), we gain insight into the behavior of integration rules for evaluating (B.2) and (B.3). We concentrate on integration rules for (B.5) since, in view of the integrand singularities at $r = 0$, these moment integrals are somewhat more challenging than their counterparts (B.4). In addition, we restrict our attention to the case $a > 0$, since for $a = 0$, both (B.3) and (B.5) equal zero for $\ell \geqslant 1$. (For $\ell = 0$, the only singularity in the functions Y_ℓ is the logarithmic singularity, which is subtracted out and resolved by integrating by parts as described in Section 3.1.)

We can now state the goal of this section more precisely: given an initial discretization and given $\varepsilon > 0$, we seek to show that there exists a number of Gaussian integration points N_{g} such that the absolute error

$$E_{N_{\mathrm{g}}} = \left|\frac{a^{\ell}}{\pi\ell}\int_a^b r^{-\ell+1}\,\mathrm{d}r - \frac{b-a}{2\ell}\sum_{j=1}^{N_{\mathrm{g}}} w_j r_j\left(\frac{a}{r_j}\right)^{\ell}\right| \tag{B.6}$$

satisfies $E_{N_{\mathrm{g}}} < \varepsilon$ for all $\ell \geqslant 0$ and for all refinements of the initial discretization. To do this, we demonstrate that (1) there exists a sufficiently large integer L such that for $\ell > L$ and for all refinements of the discretization $E_{N_{\mathrm{g}}} < \varepsilon$, *independently of* N_{g}, and (2) for $0 \leqslant \ell \leqslant L$, there exists a sufficiently large N_{g} such that $E_{N_{\mathrm{g}}} < \varepsilon$.

The proof of point (1) centers on the fact that the Gaussian sums (B.1) as well as the moment integrals (B.5) themselves decay with ℓ. Thus, for sufficiently large ℓ, although the computed moments may have large relative errors, $\delta v_\ell / v_\ell$, their absolute errors, δv_ℓ, remain smaller than ε. In more detail, bearing in mind that $w_j > 0$ and that the $\sum_{j=1}^{N_{\mathrm{g}}} w_j = \int_{-1}^{1} \mathrm{d}x = 2$ (since Gauss–Legendre quadrature integrates polynomials of degree less than $2N_{\mathrm{g}}$ exactly), we have

$$\frac{a^{\ell}}{\ell}\int_a^b r^{-\ell+1}\,\mathrm{d}r \approx \frac{b-a}{2\ell}\sum_{j=1}^{N_{\mathrm{g}}} w_j r_j\left(\frac{a}{r_j}\right)^{\ell} \leqslant \frac{b(b-a)}{\ell}, \tag{B.7}$$

where $r_j = ((b+a)/2) + ((b-a)/2)x_j$. Note that by (B.7) the first term in (B.6) decays with increasing ℓ independently of N_{g}. Clearly, by (B.5), the moment integrals themselves decays with ℓ as $\mathcal{O}(\ell^{-2})$. Thus, for L sufficiently large, $E_{N_{\mathrm{g}}} < \varepsilon$ for $\ell > L$, independently of N_{g}. We note further that refinements of the radial discretization give rise to decreases in the distance between adjacent discretization points a, b. Thus, by (B.5) and (B.7), the terms in $E_{N_{\mathrm{g}}}$ also decay with refinements of the initial discretization, thus proving point 1).

To establish point (2) we note that the error $E^{\mathrm{G}}_{N_{\mathrm{g}}}(f)$ in the integration of a function f by means of Gaussian quadrature is bounded by by [17, pp. 276–279]

$$E^{\mathrm{G}}_{N_{\mathrm{g}}}(f) \leqslant \frac{\pi}{(2N_{\mathrm{g}})!}\left(\frac{b-a}{2}\right)\left(\frac{b-a}{4}\right)^{2N_{\mathrm{g}}}\max_{a\leqslant t\leqslant b}\left|f^{(2N_{\mathrm{g}})}(t)\right|,$$

where the bound holds asymptotically as $N_{\mathrm{g}} \to \infty$. Thus, the absolute error $E_{N_{\mathrm{g}}}$ in computing (B.5) is bounded by

$$E_{N_{\mathrm{g}}} = \frac{a^{\ell}}{\pi\ell}E^{\mathrm{G}}_{N_{\mathrm{g}}}(r^{-\ell+1}) \leqslant \frac{a(b-a)}{2}\left(\frac{b-a}{4a}\right)^{2N_{\mathrm{g}}}\frac{(\ell-2+2N_{\mathrm{g}})!}{\ell(\ell-2)!(2N_{\mathrm{g}})!} \leqslant \frac{a(b-a)}{2}\left(\frac{b-a}{4a}\right)^{2N_{\mathrm{g}}}\frac{(L-2+2N_{\mathrm{g}})!}{(L-2)!(2N_{\mathrm{g}})!}.$$

Hence, if we require that $(b-a)/4a < 1$ for all pairs of points a, b in the initial discretization, then $[(b-a)/4a]^{2N_g}$ exhibits exponential decay while $(L-2+2N_g)!/(2N_g)!$ exhibits polynomial growth as N_g increases. Therefore, for N_g sufficiently large, $E_{N_g} < \varepsilon$ for $\ell \leqslant L$. Clearly, E_{N_g} remains bounded by ε with subsequent discretization refinements.

In summary, given an initial discretization satisfying $(b-a)/4a < 1$ for all pairs of points a, b, we can choose N_g sufficiently large such that the absolute error E_{N_g} in the computed moments is smaller than ε for all ℓ and for all subsequent refinements of the discretization. Similar arguments obtain the same result for the absolute error in (B.4). Note that we have only proven this fact in the asymptotic regime of large ℓ or, equivalently, small a and b. However, outside of this asymptotic regime, the Bessel functions have much milder behavior, simply oscillating with wavenumber κ. These oscillations must, in any case, be resolved by the radial discretization to obtain even minimal accuracy in solving the integral equation. Hence, computing the integral moments in the oscillatory regime presents no significant difficulties.

Although we do not present any theoretical estimates of the required values of N_g, we have found, through numerical experiments, that the value $N_g = 8$ suffices to achieve nearly machine precision accuracy in the solution for a wide range of problems. In particular, we used $N_g = 8$ in the examples of Section 6.

References

[1] O.P. Bruno, A. Sei, A fast high-order solver for EM scattering from complex penetrable bodies: TE case, IEEE Trans. Antennas Propag. 48 (12) (2000) 1862–1864.
[2] O.P. Bruno, A. Sei, A fast high-order solver for problems of scattering by heterogeneous bodies, IEEE Trans. Antennas Propag. 51 (11) (2003) 3142–3154.
[3] K.F. Warnick, W.C. Chew, Numerical simulation methods for rough surface scattering, Waves Random Media 11 (2001) R1–R30.
[4] E. Popov, M. Neviére, Grating theory: new equations in Fourier space leading to fast converging results for TM polarization, J. Opt. Soc. Am. A 17 (10) (2000) 1773–1784.
[5] L. Li, Use of Fourier series in the analysis of discontinuous periodic structures, J. Opt. Soc. Am. A 13 (9) (1996) 1870–1876.
[6] F. Seydou, Profile inversion in scattering theory: the TE case, J. Comput. Appl. Math. 137 (2001) 49–60.
[7] D. Colton, R. Kress, Inverse Acoustic and Electromagnetic Scattering Theory, second ed., Springer, Berlin/Heidelberg/New York, 1998.
[8] N.N. Bojarski, The *k*-space formulation of the scattering problem in the time domain, J. Opt. Soc. Am. 72 (1982) 570–584.
[9] P. Zwamborn, P.V. den Berg, Three dimensional weak form of the conjugate gradient FFT method for solving scattering problems, IEEE Trans. Microwave Theory Tech. 40 (1992) 1757–1766.
[10] X.M. Xu, Q.H. Liu, Fast spectral-domain method for acoustic scattering problems, IEEE Trans. Ultrasonics, Ferroelectrics Frequency Contr. 48 (2) (2001) 522–529.
[11] G. Liu, S. Gedney, High-order Nyström solution of the volume EFIE for TM-wave scattering, Microwave Opt. Technol. Lett. 25 (1) (2000) 8–11.
[12] G.M. Vainikko, Fast solvers of the Lippmann–Schwinger equation, in: R.P. Gilbert, J. Kajiwara, Y.S. Xu (Eds.), Direct and Inverse Problems of Mathematical Physics (Newark, DE 1997), International Society for Analysis, Applications and Computation, vol. 5, Kluwer Academic Publishers, Dordrecht, 2000, pp. 423–440.
[13] O.P. Bruno, E.M. Hyde, Higher-order Fourier approximation in scattering by two-dimensional, inhomogeneous media, SIAM J. Numer. Anal. (to appear).
[14] S.E. Golowich, M.I. Weinstein, Resonances of microstructured photonic waveguides and higher order homogenization expansion, Physica B 338 (2003) 136–142.
[15] E.M. Hyde, Fast, high-order methods for scattering by inhomogeneous media, Ph.D. Thesis, California Institute of Technology, 2003 (defended August 14, 2002).
[16] W.H. Press, S.A. Teukolsky, W.T. Vetterling, B.P. Flannery, umerical Recipes in Fortran 77: The Art of Scientific Computing, vol. 1, second ed., Cambridge University Press, Cambridge/New York, 1992.
[17] K.E. Atkinson, An Introduction to Numerical Analysis, second ed., Wiley, New York, 1989.
[18] Netlib repository. Available from <http://www.netlib.org>.
[19] A. Greenbaum, Iterative Methods for Solving Linear Systems, Frontiers in Applied Mathematics, vol. 17, SIAM, Philadelphia, 1997.
[20] D. Gilbarg, N.S. Trudinger, Elliptic Partial Differential Equations of Second Order, Springer, Berlin/Heidelberg/New York, 1977.
[21] G.H. Golub, C.F.V. Loan, Matrix Computations, third ed., The Johns Hopkins University Press, Baltimore, London, 1996.